



# Melting of siderite to 20 GPa and thermodynamic properties of FeCO<sub>3</sub>-melt



Nathan Kang<sup>a,\*</sup>, Max W. Schmidt<sup>a</sup>, Stefano Poli<sup>b</sup>, Ettore Franzolin<sup>a</sup>, James A.D. Connolly<sup>a</sup>

<sup>a</sup> Department of Earth Sciences, Institute of Geochemistry and Petrology, ETH, 8092 Zurich, Switzerland

<sup>b</sup> Dipartimento di Scienze della Terra, Università degli Studi di Milano, Via Botticelli 23, 20133 Milano, Italy

## ARTICLE INFO

### Article history:

Received 19 May 2014

Received in revised form 8 January 2015

Accepted 5 February 2015

Available online 14 February 2015

Editor: D.B. Dingwell

### Keywords:

Siderite

Oxidation

Carbon cycle

Melting

Phase equilibrium

Thermodynamic properties

## ABSTRACT

The siderite (FeCO<sub>3</sub>) melting curve is determined through multi-anvil experiments at 6–20 GPa, and 1300–1870 °C. The experiments define a melting curve with a Clapeyron slope steepening from 45 to 18 °C/GPa but without backbend at upper mantle conditions, i.e., siderite is denser than FeCO<sub>3</sub>-melt (FeCO<sub>3</sub>L). The melting curve fits  $T_m = 1037(44) + 70.0(88) * P - 1.43(37) * P^2$  (valid from 5 to 20 GPa) where pressure is in GPa and temperature in °C. Siderite melting is not stoichiometric, minor quench magnetite was always observed and is interpreted as the result of partial redox dissociation of FeCO<sub>3</sub>L leading to dissolved Fe<sup>3+</sup> and CO<sub>2</sub> in the carbonate melt. At pressures below ~6.8 GPa, siderite does not melt but decomposes through an auto redox dissociation reaction to magnetite, a carbon polymorph and CO<sub>2</sub>. From the experimental determination of the pure siderite melting curve, we calculate thermodynamic properties of the FeCO<sub>3</sub>L end-member, which reproduce the siderite melting curve in *P*–*T* space better than 10 °C. The metastable 1 atm melting temperature is calculated to 1012 °C. Siderite has the lowest melting temperature of the Ca–Mg–Fe carbonates, its melting curve may cross the mantle geotherm at transition zone pressures. The stability of siderite is not only dependent on pressure and temperature but also strongly on oxygen fugacity (*f*O<sub>2</sub>). Model calculations in *P*–*T*–*f*O<sub>2</sub> space in a Fe–C–O<sub>2</sub> system show that the siderite or FeCO<sub>3</sub>-melt maximum stability is always reached at conditions of the CCO buffer. Our experimental and thermodynamic data constitute a cornerstone to model carbonate melting in the deep Earth, necessary to understanding the deep carbon cycle.

© 2015 Elsevier B.V. All rights reserved.

## 1. Introduction

Carbon is a major and vital component in the geological rock record. It occurs in oxidized form as CO<sub>2</sub> and carbonate, as elemental carbon (graphite or diamond) and metallic phases (e.g., Fe<sub>3</sub>C), or in its reduced state, mostly as organic material but also as CH<sub>4</sub> or hydrocarbon species in reduced fluids. The majority of the Earth's surface carbon is sequestered in carbonates contained either in sedimentary rocks or in the altered oceanic crust. Ocean floor metamorphism enriches the oceanic crust with CO<sub>2</sub> through precipitation of carbonates (Staudigel, 2003). The transport and storage of carbon within the mantle influence the global carbon budget via volcanic CO<sub>2</sub> release to the atmosphere and subsequent cycling back into the mantle by subduction of oceanic sediments and carbonated peridotitic and mafic rocks (Sleep and Zahnle, 2001). In general, most of the subducted carbonate is believed to descend beyond subarc depth, this in contrast to hydrous phases, whose larger part decomposes and generates H<sub>2</sub>O-rich fluids at subarc conditions (Connolly, 2005; Poli et al., 2009). As a result, carbon-bearing minerals are transferred to deeper mantle regions. These are

documented as carbonate inclusions in natural diamonds (e.g. magnesite) and carbonate minerals in mantle xenoliths (Pal'yanov et al., 1999).

The modern C-cycle is characteristic for an Earth with an oxygen-rich atmosphere. Before the first rise of oxygen ~2.3 Ga ago, lithologies such as banded iron formations (BIFs) and anoxic shales were much more abundant and constituted common deep sea and platform sediments of anoxic oceans (Klemm, 2000). BIFs, mostly composed of quartz + hematite + magnetite are frequently also rich in organic carbon (Beukes and Gutzmer, 2008). The latter reacts with the iron oxides upon low grade metamorphism to siderite (FeCO<sub>3</sub>) or ankerite (CaFe(CO<sub>3</sub>)<sub>2</sub>). Most of these ancient sediments, especially deep sea BIFs, were subducted in the Archean (Kusky et al., 2001; Polat et al., 2002). To understand this process, the high-pressure behavior of siderite needs to be characterized. The “pure”, simple BIF system SiO<sub>2</sub>–FeO–Fe<sub>2</sub>O<sub>3</sub> is refractory and melts only at 1455 °C at 1 atm (Phillips and Muan, 1959). The addition of carbon and hence of siderite or ankerite is expected to strongly reduce such melting temperatures.

Understanding carbonate stability at mantle conditions is also crucial under other aspects: First, for the carbon cycle itself, secondly, because at high pressures carbonate-bearing silicate rocks have lower melting temperatures than those with only silicates, and third, because

\* Corresponding author. Tel.: +41 44 63 23789.

E-mail address: [nathan.kang@erdw.ethz.ch](mailto:nathan.kang@erdw.ethz.ch) (N. Kang).

carbonatitic magmas are highly mobile and enriched in trace elements, their transfer modifying the geochemistry of deep mantle domains. In this context, the  $\text{CaCO}_3\text{--MgCO}_3\text{--FeCO}_3$  ternary constitutes the most basic system for carbonates and carbonate melts and is a key to predict melting relations even in any more complex system, since natural carbonatites are dominated by (Ca, Mg,  $\text{Fe}^{2+}$ )-components.

The first experimental study in the Ca–Mg–Fe-carbonate ternary described subsolidus phase relations at 600–800 °C, 1.5 GPa (Goldsmith et al., 1962). Below 700 °C, Goldsmith et al. (1962) determined a 3-phase field consisting of coexistent Fe–dolomite, Fe–calcite and Mg–siderite. Furthermore, Rosenberg (1967) investigated this ternary at temperatures between 350 and 550 °C at 0.2–0.3 GPa and confirmed the presence of the above 3-phase field. Finally a complete ternary solid solution model for carbonates to 1100 °C, 3.5 GPa was formulated by Franzolin et al. (2011) on the basis of additional experiments.

Regarding end-members of the  $\text{CaCO}_3\text{--MgCO}_3\text{--FeCO}_3$  system, Irving and Wyllie (1975) experimentally constrained the melting reaction of pure calcite at 1, 2 and 3 GPa to ~1430, 1550 and 1610 °C. Suito et al. (2001) determined  $\text{CaCO}_3$  melting temperatures of ~1730 °C at 4–6 GPa and ~2000 °C at 8 GPa and proposed a melting curve for disordered calcite. Congruent melting of pure magnesite is observed at 1585 to 1620 °C at 3 to 3.6 GPa (Irving and Wyllie, 1975) and at 8 to 15 GPa at ~1950 and ~2050 °C, respectively (Katsura and Ito, 1990). Note that these data suggest that the calcite and magnesite melting curves cross at ~5 GPa.

Experimental data on the phase relationships of siderite at high pressure are limited and thermodynamic data of melt of siderite composition ( $\text{FeCO}_3\text{L}$ ) are completely lacking. The system Fe–C– $\text{O}_2$  has been studied experimentally to 1.5 GPa and 700 °C (French, 1971; Weidner, 1972; Koziol, 2004). More recently, Tao et al. (2013) investigated the siderite stability field to 10 GPa by multi-anvil experiments. For comparison, calcite melt becomes stable at pressures greater than a few hundred bar, magnesite melt only stabilizes at  $\geq 2.7$  GPa (Irving and Wyllie, 1975), while siderite melt requires between 7 and 8 GPa (Tao et al., 2013).

The present study provides experimental data for the siderite system from 6 to 20 GPa in the temperature range of 1300–1870 °C. The purpose is to understand the stability of siderite as a function of oxygen fugacity and to constrain the thermodynamics of  $\text{FeCO}_3\text{L}$ . The  $\text{FeCO}_3\text{L}$  data can be applied e.g. to predict the melting behavior of carbonated banded iron formations, an alkali-free, chemically relative simple system, which once was that of a common sediment.

## 2. Previous experimental phase relations of Fe-rich carbonates and siderite

Phase equilibria in the Fe–C– $\text{O}_2$  system (Fig. 1) have been investigated by few experimental studies aiming at the origin of Fe-rich carbonatites and at BIFs and their metamorphosed equivalents. Siderite is a common constituent of low-grade sedimentary iron formations and hydrothermal veins. Most natural siderites contain significant amounts of  $\text{Mg}^{2+}$  and  $\text{Mn}^{2+}$  and are commonly associated with iron-rich dolomite or ankerite. Upon thermal dissociation of carbonates such as calcite, magnesite and smithsonite ( $\text{ZnCO}_3$ ), their cations do not oxidize (Harker and Tuttle, 1955). However, several investigations show that siderite is not stable under atmospheric conditions (Smythe and Dunham, 1947; Holland, 1965; Seguin, 1966; French, 1970). Natural siderite converts to iron oxides or hydroxides upon exposure to the atmosphere or to near-surface ground waters (Silliman, 1820; Burchard, 1924). In the Fe–C–O system siderite may either decompose through a simple decarbonation reaction:

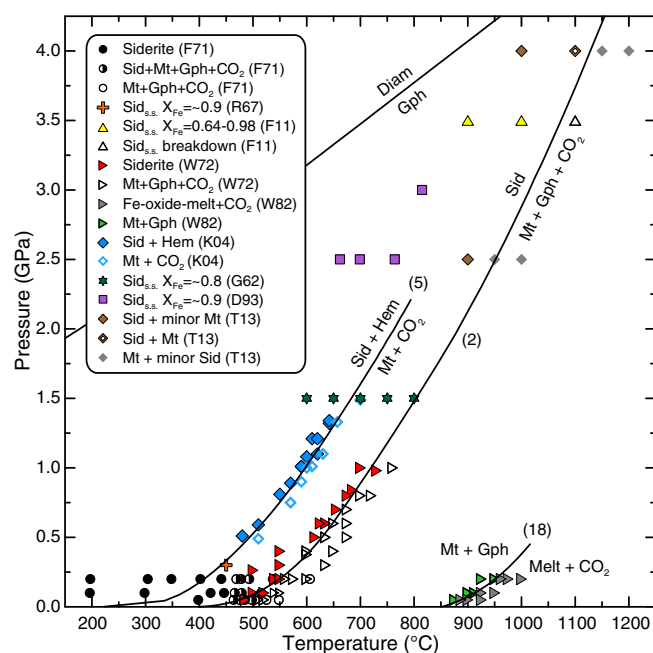


**Fig. 1.** P–T diagram compiling subsolidus experiments on siderite, also including the few experiments on Ca–Mg–Fe carbonates and calcite–siderite solid solutions with  $X_{\text{Fe}} = 0.64\text{--}0.98$ . The terminal stability of siderite is defined by redox dissociation to magnetite + graphite +  $\text{CO}_2$  (reaction 2, the curve is a visual fit to the data). Reaction 5 is calculated with our siderite data. Weidner (1982) determined the low pressure minimum melting reaction (18) in Fe–C–O at low pressures. F71: French, 1971, R67: Rosenberg, 1967, F11: Franzolin et al., 2011, W72: Weidner, 1972, W82: Weidner, 1982, K04: Koziol, 2004, G62: Goldsmith 1962, D93: Davidson et al., 1993, T13: Tao et al., 2013. Hem = hematite; Sid = siderite; Sid<sub>ss</sub> = siderite solid solution; Mt = magnetite; Gph = graphite; Diam = diamond; C = carbon;  $\text{FeCO}_3\text{L}$  = melt of almost  $\text{FeCO}_3$  composition; Lc = carbonate quench; AuPd = gold–palladium capsule alloy; Wu = wüstite; IronL = iron melt; HM = hematite–magnetite buffer; CCO = graphite– $\text{CO}_2$  buffer; MW = magnetite–wüstite buffer; WI = wüstite–iron buffer. (Color online.)

or through a redox-dissociation reaction:

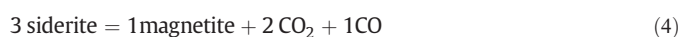


(Fig. 1), this latter univariant reaction delimits siderite stability at low pressures. Reaction 2 was studied by French (1971) in the system Fe–C– $\text{O}_2$  between 50 and 200 MPa in a  $\text{CO}_2 + \text{CO}$  atmosphere as a function of T,  $P_{\text{F}} (= P_{\text{CO}_2} + P_{\text{CO}})$ . Further high pressure cold-seal experiments on this reaction were conducted by Weidner (1972) from 0.05 to 1 GPa and 450 to 760 °C, employing pure siderite as a starting material. The equilibrium curve (reaction 2) is characterized by a slight change in slope at ~0.45 GPa and 600 °C, which was interpreted as a non-quenchable polymorphic transformation in siderite (Weidner, 1972). Most recently, reaction 2 was determined at 2.5–6 GPa where it has a Clapeyron slope of about 0.0082 GPa/K (Tao et al., 2013). This latter study found siderite + magnetite to melt at 1500 °C, 8 GPa and 1550 °C, 10 GPa.

Equilibrium reaction 2 constrains oxygen fugacity to the CCO buffer, which implies that CO may occur as a species, either via the equilibrium



or directly through decomposition of siderite



(French and Rosenberg, 1965). Nevertheless, the molar fraction of CO at high-pressure conditions is vanishingly small and calculated to be  $0.29 \times 10^{-3}$  at 10 GPa, 1500 °C, such that CO will no longer be discussed here.

A further reaction that has importance consequences for the stability of siderite is



Kozioł (2004) determined the equilibrium curve of reaction 5 in the range 0.5–1.4 GPa, 480–700 °C by piston-cylinder experiments (Fig. 1). Silver oxalate ( $\text{Ag}_2\text{C}_2\text{O}_4$ ) was used as a  $\text{CO}_2$  source and oxygen fugacity was buffered to hematite–magnetite (HM). Reaction progress was observed by the extent of  $\text{CO}_2$  gas loss and by X-ray diffraction analysis (Kozioł, 2004).

In the Fe-rich corner of the Ca–Mg–Fe carbonate ternary, experimental data are limited to the subsolidus stability of siderite solid solution (siderite<sub>s.s.</sub>). Rosenberg (1967) found stable siderite<sub>s.s.</sub> with  $X_{\text{Fe}} = 0.9$  at 450 °C and 0.3 GPa (Fig. 1) using cold seal pressure vessels. The stability of siderite<sub>s.s.</sub> with  $X_{\text{Fe}} = 0.8$  was determined by Goldsmith et al. (1962) in a “squeezer”-type apparatus (Griggs and Kennedy, 1956) between 600 and 800 °C at 1.5 GPa. At higher pressures (3.5 GPa)  $\text{Ca}_{0.525}\text{Fe}_{0.475}\text{CO}_3$  coexists with siderite ( $X_{\text{Fe}} = 0.98$ ) at 900 °C and complete miscibility was observed along the join  $\text{CaCO}_3$ – $\text{FeCO}_3$  at 1000 °C (Franzolin et al., 2011). At 1100 °C and 3.5 GPa, Fe-rich ankerite is not stable anymore and breaks down to magnetite + ankerite + graphite (Franzolin et al., 2011). On the join  $\text{CaCO}_3$ – $\text{FeCO}_3$ , Davidson et al. (1993) found that siderite<sub>s.s.</sub> with  $X_{\text{Fe}} \sim 0.9$  coexists with calcite<sub>s.s.</sub> in the temperature interval of 660–760 °C and at pressures of 2.5–3 GPa.

### 3. Experimental and analytical techniques

#### 3.1. Starting materials

Starting materials of almost all multi-anvil experiments consisted of homogenous powders of synthetic siderite ( $\text{FeCO}_3$ ). Only the first experiment at 10 GPa, 1600 °C was run on a natural siderite ( $X_{\text{Fe}} = 0.947$ ) from Greenland. Each sample capsule was loaded with a small graphite piece to ascertain that the internal  $f_{\text{O}_2}$  did not exceed that of the CCO buffer. Synthetic siderite was preferred over natural siderite because of the common oxidation along the cleavage of natural crystals and the presence of other divalent cations (in particular Mn) in natural siderite. A method of siderite synthesis involving decomposition of ferrous oxalate dihydrate ( $\text{FeC}_2\text{O}_4 \cdot 2\text{H}_2\text{O}$ ) has been adopted from earlier work (Rosenberg, 1963; French, 1971; Weidner, 1972). We sealed iron oxalate dihydrate into 4.7 cm long gold capsules with 5.4 mm outer diameter. The sample was heated to and held at 350 °C and 200 MPa in an externally heated cold seal vessel for 120 h following French (1971). The resultant siderite was a gray–white very slightly brownish crystalline powder and analyzed by SEM (scanning electron microscope) and XRD (X-ray diffraction). Siderite was stored permanently at ambient temperature in a glass desiccator to slow oxidation. Still, it was synthesized repeatedly as even in a desiccator synthetic siderite develops an intensive brown color with time, identified to stem from oxidation products forming on the surface of the siderite crystals.

#### 3.2. Experimental procedure and methods

High pressure experiments (Table 1) were performed at 6, 10, 13.6 and 20 GPa in 600 and 1000-ton presses loaded with the same Walker-type multi-anvil device. 32 mm tungsten carbide (WC) cubes were used as second stage anvils, gaskets were made of natural pyrophyllite. An 18/11 assembly was used to 6 and 10 GPa (18 mm edge length  $\text{Cr}_2\text{O}_3$  doped MgO-octahedra, 11 mm truncation edge length of WC cube, calibrated against the coesite–stishovite), (Yagi and Akimoto, 1976; Zhang et al., 1996) and  $\text{CaGeO}_3$  garnet–perovskite transitions (Susaki et al., 1985), a 14/8 assembly for 13.6 GPa, calibrated against coesite/stichovite and forsterite/wadsleyite, (Morishima et al., 1994) and a 10/3.5 assembly for 20 GPa (for calibration see Stewart

**Table 1**

Experimental run conditions and phase assemblages. All experiments had a graphite chip added to assure buffering to CCO.

Sample #	P (GPa)	T (°C)	Run time (min)	Run products (proportion in %)
E-1	6	1300	90	Sid (100)
E-2	6	1350	60	Sid (100)
E-3	6	1400	60	Sid (89) + Mt (11)
E-4	6	1450	75	Mt + Gph + ( $\text{CO}_2$ )
pS-02	10	1500	20	Sid (100)
pS-03	10	1530	20	Sid (91.5) + M (8.5) + B?
pS-01	10	1600	20	Sid (29.8) + M (70.2)
pS-04	10	1670	20	Sid (1.8) + M (98.2) + B
pS-05	13.6	1550	20	Sid (100)
pS-06	13.6	1600	20	Sid (92) + M (8)
pS-07	13.6	1700	20	Sid (2.3) + M (97.7)
ps20-1	20	1550	20	Sid (100)
ps20-5	20	1600	20	Sid (100)
ps20-8	20	1650	20	Sid (100)
ps20-3	20	1675	20	Sid (94.2) + M (5.8)
ps20-2	20	1725	20	Sid (85.8) + M (14.2)
ps20-7	20	1750	20	Sid (84.6) + M (15.4)
ps20-9	20	1800*	5	Sid (44.5) + M (55.5)
ps20-10	20	1870	5	Sid (39.6) + M (60.4)

Notes: Sid = siderite; Mt = magnetite; Gph = graphite; M = melt; B = bubble (not considered in phase proportions, for further information see text). Phase proportions in parentheses are estimated by visual determinations from the BSE images. \*thermocouple breakage during experiment, final temperature uncertain.

et al. (2006)). Assemblies for experiments at 6 GPa contained stepped graphite furnaces, for the other experiments we used stepped (10 and 14 GPa) or straight (20 GPa)  $\text{LaCrO}_3$  heaters. The 18/11 and 14/8 assemblies contained axial thermocouples while the 10/3.5 assembly has a thermocouple running across the center of the furnace (Stewart et al., 2006). The assemblies consisted further of  $\text{ZrO}_2$  thermal insulation sleeves, internal MgO spacers and a molybdenum end ring and disc ensuring electrical contact between assembly and WC cubes. Welded Pt–C double capsules were used for siderite experiments at 6 GPa, at higher pressures we employed either  $\text{Au}_{80}\text{Pd}_{20}$  or  $\text{Au}_{50}\text{Pd}_{50}$  capsules, the latter if higher temperatures (i.e.  $\geq 1850$  °C) required their use. Temperature was measured with a B-type (18/11 and 14/8) or C-type ( $\text{WRe}_5$ – $\text{WRe}_{26}$ ; for 10/3.5) thermocouple and controlled by a Eurotherm controller. Experiments were quenched at a rate of  $\sim 800$  °C/s by shutting of the power supply. Pressure was gradually unloaded for more than 12 h. The temperature precision including temperature gradients within the capsule are 15–30 °C in 18/11 and 14/8 experiments. Temperature gradients within the 10/3.5 assembly are  $\sim 50$  °C across the capsule length of  $\sim 1.2$  mm (details for the 10/3.5 assembly by Stewart et al., 2006).

#### 3.3. Analytical techniques

Recovered sample capsules were longitudinally embedded in epoxy resins, ground and then polished with diamond paste to expose a level along the axis of the capsule. Textural relationships between phases were examined by back-scattered electron (BSE) imaging using a JEOL JSM 6390LA scanning electron microscope equipped with an EDX for analyzing phase compositions.  $\text{CO}_2$  contents of the carbonates were calculated by stoichiometry. Micro-Raman spectroscopy (Horiba Jobin Yvon LabRam HR 800) was used additionally to identify the nature of oxide and carbonate phases.

### 4. Results

In total, 19 successful experiments were performed on synthetic  $\text{FeCO}_3$  buffered close to graphite–CO– $\text{CO}_2$  (CCO) at 6, 10, 13.6 and 20 GPa, and temperatures of 1300–1870 °C (Table 1). Characteristic textural features of the experimental charges are shown in Fig. 2. The

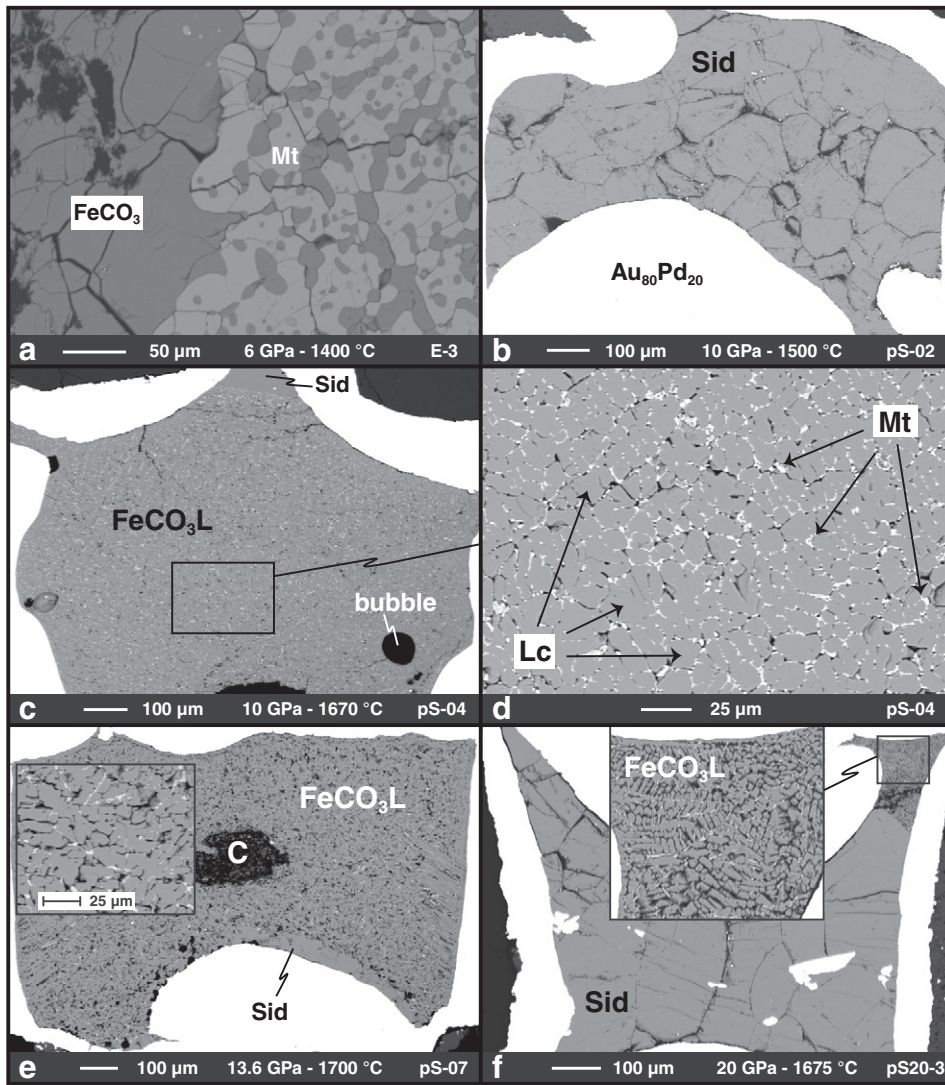


**Fig. 2.** Back-scattered electron (BSE) images of experimental charges showing subsolidus, partial melting and almost fully molten assemblages. (a) Siderite at subsolidus conditions with partial decomposition to magnetite and (b) a monomineralic stable siderite assemblage. (c) Liquidus condition at 10 GPa with mostly FeCO<sub>3</sub>L that shows a gas bubbles interpreted as coexisting CO<sub>2</sub>-fluid. Note the tiny amount of siderite crystals at the top, corresponding to the cold end of the capsule, and thought to persist because of the temperature gradient across the capsule. (d) Magnetite is interstitial to the dendritic siderite quench crystals phases. (e) FeCO<sub>3</sub>L at liquidus conditions showing the small added chip of graphite, now transformed to micro-diamond. (f) Beginning of melting at 20 GPa. Abbreviations as in Fig. 1.

siderite melting curve in the Fe–C–O system is shown in Fig. 3 as constrained by the experimental brackets of this study and of Tao et al. (2013). Direct melting of siderite is stable at pressures above ~6.8 GPa, at the invariant point, siderite is in equilibrium with FeCO<sub>3</sub>L, magnetite, diamond and CO<sub>2</sub>-fluid.

An unfortunate feature of siderite-rich systems is that phase relations in the FeCO<sub>3</sub> sub-system cannot be described by a single thermodynamic component because both the auto-redox-dissociation (reaction 2) to magnetite + C + CO<sub>2</sub> and the simple decarbonation (reaction 1) to wüstite + CO<sub>2</sub> operate at melting temperatures. These reactions are unavoidable and are probably the reason that little experimental information is available on siderite melting.

#### 4.1. Textures of the run products

Subsolidus assemblages and domains with crystals in supersolidus experiments are characterized by marked 120° triple junctions, homogeneous phase compositions, completely reacted starting materials and

pronounced grain growth of carbonate crystals (Fig. 2). In subsolidus experiments siderite crystals form 100–200 μm polyhedral grains. In partly molten charges, carbonate melts were always assembled in the hotspot of the capsule and form large pools. Carbonate melts are not quenchable and are characterized by an intergrowth of carbonate needles and feather crystals with dendritic textures. The needles and feather crystals generally contain interstitial (quench) iron oxides, probably magnetite and/or wüstite. In experiments with high melt fractions large gas bubbles were observed in equilibrium with carbonate melt.

#### 4.2. Temperature stability and melting of siderite

The siderite melting reaction



was experimentally bracketed at 10, 13.6 and 20 GPa (Fig. 3). A first fraction of FeCO<sub>3</sub>-dominated melt formed between 1500 and 1530 °C

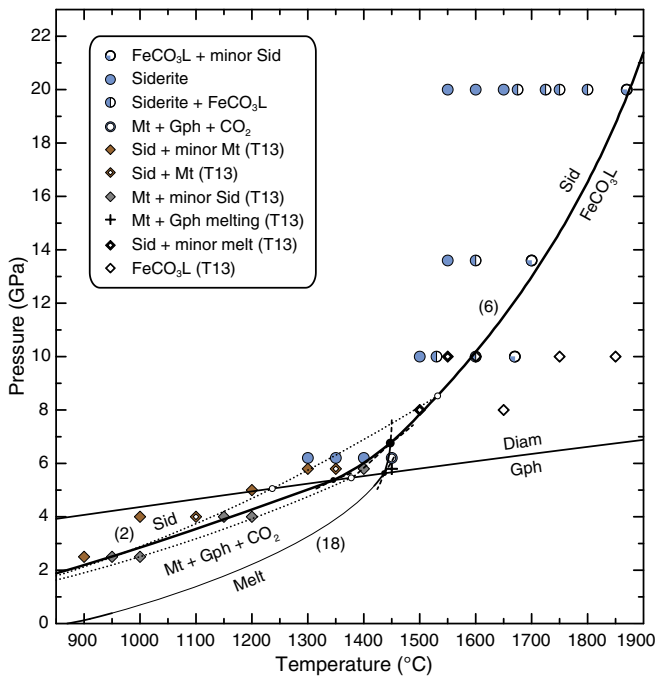
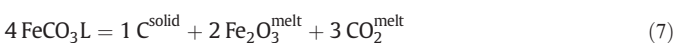


**Fig. 3.** Melting relations of siderite. The melting curve is stable from the invariant point (black circle) at ~6.8 GPa to > 20 GPa. Siderite melting occurs over a wide interval, the disappearance of siderite is taken to define the melting curve. The melting curve (6) is shown as calculated with our thermodynamic properties of  $\text{FeCO}_3\text{L}$ . The siderite decomposition curve to magnetite + graphite +  $\text{CO}_2$  (reaction 2) is drawn to fit the experimental brackets. The upper pointed line represents the calculated position of this reaction employing the fluid EoS for  $\text{CO}_2$  after Pitzer and Sterner (1994) as adopted by Holland and Powell (2011). The lower pointed curve shows the calculated position of reaction 2 using the fluid EoS for  $\text{CO}_2$  after Saxena and Fei (1987). Melting in this system at <6.8 GPa involves magnetite + graphite +  $\text{CO}_2$  as educts (reaction 18). This reaction should connect to the low pressure melting curve of Weidner (1982, bold line at 0.05–0.2 GPa), but note that the  $\text{CO}_2$  solubility in the melt and reaction stoichiometry will strongly change along this reaction. Dashed lines represent metastable prolongations of reactions. Small white circles are invariant points that would arise from the calculated reaction 2. All symbols near 6 GPa represent experiments at 6 GPa (Tao et al., 2013 and this study), but are not superimposed for clarity. Abbreviations as in Fig. 1.

at 10 GPa, 1550–1600 °C at 13.6 GPa and 1675 °C at 20 GPa. Almost complete melting was achieved between 1600 and 1670 °C at 10 GPa, at 1700 °C at 13.6 GPa and near 1870 °C at 20 GPa.

At lower pressures ( $\leq 6$  GPa) siderite decomposed according to reaction 2 before melting. Experiments at 6 GPa yield siderite at 1400 °C, but siderite completely decomposed through auto-redox dissociation (reaction 2) at 1450 °C. The high  $\text{CO}_2$ -yield of this reaction often led to experimental failures with broken capsules or highly porous run products. At higher pressures, between 10 and 20 GPa, experiments on siderite show near congruent melting leading to coexisting siderite crystals and  $\text{FeCO}_3\text{L}$ . In these experiments, siderite was well-crystallized with large prismatic grains of 200–320  $\mu\text{m}$  size at temperatures of 1500–1870 °C. Quenched  $\text{FeCO}_3\text{L}$  is characterized by textural features as a mixture of dendritic or feather-like carbonate crystals and minor oxide quench components suggesting that the melt is not stoichiometric  $\text{FeCO}_3$ , but contains some ferric component (Fig. 2c–f).

It is important to acknowledge that a system with  $\text{FeCO}_3$  composition represents a pseudo-unary system, in reality constituted by the three components FeO, C, and  $\text{O}_2$ . The analog to siderite redox dissociation (reaction 2) within the melt phase can be represented in terms of hypothetical melt species and graphite as



or, if  $\text{CO}_2$  is recast as a putative  $\text{Fe}^{3+}$ -carbonate species



It is unknown whether the  $\text{CO}_2$  resulting from the redox dissociation dissolves as molecular species or as carbonate group (charge balanced by  $\text{Fe}^{3+}$ ) but from the stoichiometry of reactions 7 and 8 it is clear that some ferric iron must be dissolved as oxide component in  $\text{FeCO}_3\text{L}$ . If one assumes that elemental carbon is not soluble in a carbonate-oxide melt, the true melt composition in a two-phase graphite + melt system must lie on the prolongation of the tie line graphite–siderite (thick line, Fig. 4). From image analysis, the proportion of bright quench phases in BSE images of the melt was determined to ~5–7% (e.g. Fig. 2d) by using ImageJ histogram analysis (Schneider et al., 2012). These bright phases interstitial to the carbonate feather crystals (Fig. 2f) are oxides that probably represent the ferric iron dissolved in the melt. Accordingly, we suggest that less than 10% of the Fe in the melt is ferric.

Furthermore, in some of the high temperature experiments, large bubbles in the melt (Fig. 2c) indicate exsolution of a fluid from the melt, suggesting that the  $\text{CO}_2$  produced in reaction 7 has a limited solubility in  $\text{FeCO}_3\text{L}$ . In such a three-phase system, the melt would move slightly to the magnetite side of the thick blue line in Fig. 4.

## 5. Location of the siderite melting reaction

The determination of the equilibrium temperature of the unary model melting reaction 6 is complicated by the fact, that the temperature between the first appearance of melt (Fig. 2f) and the disappearance of siderite is 50 to 150 °C, increasing with increasing pressure. This large melting interval (also observed by Tao et al., 2013) is best explained by (i) the presence of additional components and (ii) the melt composition being slightly different from  $\text{FeCO}_3$  (through precipitation of graphite or diamond and exsolution of  $\text{CO}_2$  at the higher temperatures).

In general, a small (i.e. in the order of 1%) amount of additional components may lower the solidus temperature of a system enormously but modifies the liquidus temperature by a small amount. This is best

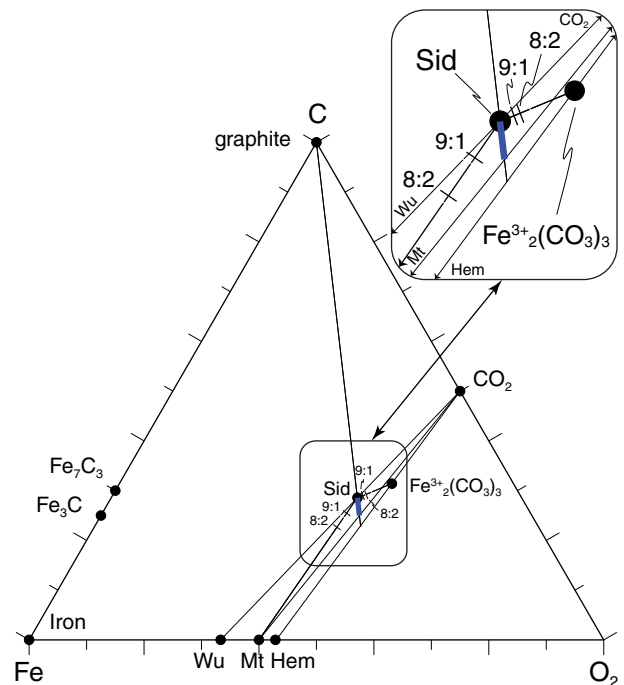


**Fig. 4.** Chemography of the Fe–C– $\text{O}_2$  system. Precipitating graphite/diamond,  $\text{FeCO}_3\text{L}$  moves away from the graphite-apex and contains a ferric iron and a  $\text{CO}_2$  component. Image analysis indicates <10% of quench oxide. For details see text.

illustrated in the albite system where a small amount of water suppresses the dry liquidus (~1250 °C at 1 GPa) by less than a few tens of degrees, while the same amount of H<sub>2</sub>O lowers the solidus to ~700 °C (Burnham and Davis, 1974). Similarly, 0.4 wt.% water has a large effect on the mantle solidus, lowering the melting temperature by ~500 °C at 3 GPa (Wyllie, 1979). In contrast, the influence of H<sub>2</sub>O on the liquidus is much less, in case of a basaltic melt, the liquidus depression is only ~20 °C with 0.5 wt.% H<sub>2</sub>O in the melt (Medard and Grove, 2008). In our study, additional components result from the disproportionation reactions 7 and 8; also some residual absorbed moisture may be present, which cannot be dried off at the 110 °C permitted for drying siderite, higher temperatures leading to its oxidation. A few siderite crystals in the almost completely molten samples pS-04, pS-07 and ps20-10 (Fig. 2c,e) are interpreted to result from the temperature gradient within the sample capsule. We have thus taken the almost complete disappearance of siderite as its melting temperature. The resulting melting reaction steepens slightly with pressure but maintains a positive Clapeyron slope of 45 to 18 °C/GPa (10–20 GPa), the melt remaining always less dense than the crystals at upper mantle conditions.

We combine the experimental data of this study and those from Tao et al., 2013 on siderite melting yielding a total of four brackets at 8, 10, 13.6 and 20 GPa. A fifth artificial bracket at 5 GPa is derived from the fact that in *P*–*T* space the metastable prolongation of the siderite melting curve must pass between equilibrium 2 and the magnetite + graphite + CO<sub>2</sub> – melting curve (Fig. 3, see also Section 7.2.3). These brackets constrain the siderite liquidus to the quadratic polynomial

$$T_m = 1037(44) + 70.0(88) * P - 1.43(37) * P^2 \quad (9)$$

(with *P* in GPa, *T* in °C, errors are 1  $\sigma$ ). This curve in combination with the available data on siderite is then used to derive the thermodynamic properties of FeCO<sub>3</sub>L.

## 6. Thermodynamic properties of FeCO<sub>3</sub>L

Thermodynamic melt solution models to calculate melting relations have been proposed e.g. for broadly basaltic silicate melts (Ghiorso and Sack, 1995) and for granitic melts (Holland and Powell, 2001; Gualda et al., 2012). A melt model for carbonate melts is presently lacking. Here, we calculate the thermodynamic properties for a hypothetical end-member FeCO<sub>3</sub>L. Although the Fe<sup>2+</sup> oxidation shifts the melt composition slightly away from pure FeCO<sub>3</sub> during the experiment, we take melting reaction 6 as congruent, acknowledging that this melt contains a minor Fe<sup>3+</sup> component and hence some dissolved CO<sub>2</sub> in excess of a M<sup>2+</sup>CO<sub>3</sub> stoichiometry.

### 6.1. Choice of *C<sub>p</sub>*

There is a broad range of strategies regarding *C<sub>p</sub>* functions of liquids. Although many experimentally derived heat capacities for stable and supercooled liquids are temperature independent (Richet and Bottinga, 1980; Marcus, 2009), a theoretical approach on molten salts suggests existence of temperature dependence, e.g. Eq. (8) in Marcus (2009). Thermodynamic modeling of silicate liquids currently adopt constant heat capacities at the temperature of interest (Berman and Brown, 1985; Ghiorso and Sack, 1995), but, in the absence of experimentally constrained properties, thermodynamic data for liquids used in material science (Bale et al., 2002) adopt *C<sub>p</sub>* functions identical to the solids.

We have tested a constant *C<sub>p</sub>*(*T*), a *C<sub>p</sub>*(*T*) identical to the solid, a *C<sub>p</sub>* increased by a constant (fitted) value with respect to the two former approaches, and a *C<sub>p</sub>* function for the liquid phase, that reproduces the Dulong–Petit limit

$$C_p = 3 * R * n + \alpha_T^2 * V_T * K_T * T \quad (10)$$

where *R* is the gas constant and *n* the number of atoms in the substance of interest. We found that this latter approach yields the most reasonable volumetric properties along the melting curve, in particular a continuously increasing Clapeyron slope without a backbend (i.e. a denser liquid) for which there is no experimental evidence.

### 6.2. Volumetric properties of carbonate melts

The compressibilities of carbonate melts are not well constrained. Molten salts show a very low 1 bar bulk modulus, six to eight times lower than corresponding crystalline solids (Marcus, 2013). Liu et al. (2007) used the *K<sub>0</sub>* for K<sub>2</sub>CO<sub>3</sub> of 3.8 GPa as determined at 1 bar, 1500 °C by sound speed measurements (Zhu et al., 1991). Including own experimental data on K<sub>2</sub>CO<sub>3</sub>-melting which yielded 1175–1200 °C at 1.86–3.16 GPa and data from Klement and Cohen (1975) at 0.08–0.44 GPa, Liu et al. argue that the bulk modulus rapidly increases to 33 GPa at a pressure of 4 GPa. The best fit to a Birch–Murnaghan EoS yielded a *K'* of 13.7 (Liu et al., 2007) and hence a backbend of the fusion curve of K<sub>2</sub>CO<sub>3</sub> at ~2.6 GPa and a negative Clapeyron slope at higher pressures. Such a backbend would be inconsistent with the melting temperature of K<sub>2</sub>CO<sub>3</sub> of 1400–1450 °C at 6 GPa by Shatskiy et al. (2013), at least as long as there is no evidence for any phase transition of the solid. The melting curves of calcite and magnesite were determined from 0.1 to 6 GPa for calcite (Wyllie and Tuttle, 1960; Irving and Wyllie, 1975; Suito et al., 2001) and from 2.75 to 15 GPa for magnesite (Irving and Wyllie, 1975; Katsura and Ito, 1990). In these two cases, the solids are known to not undergo any phase transition at the conditions of the above melting curves. These melting curves have positive Clapeyron slopes, indicating that CaCO<sub>3</sub>L and MgCO<sub>3</sub>L remain less dense than the solid at these pressures. In summary, all known high-pressure melting curves of carbonates steepen with pressure but there is no experimental evidence that the volume change of melting changes sign in the pressure range studied. Sound speed measurements on mixed K<sub>2</sub>CO<sub>3</sub>–Na<sub>2</sub>CO<sub>3</sub>–Li<sub>2</sub>CO<sub>3</sub>–CaCO<sub>3</sub> liquids were performed at 1 bar under a CO<sub>2</sub> atmosphere from 725 to 1242 K (O'Leary et al., 2009) suggesting that *K'* of liquid CaCO<sub>3</sub> has a value of ~7 ± 1.

The siderite structure remains stable to at least 50 GPa, 1700 °C (Santillan and Williams, 2004; Litasov et al., 2013), above 60 GPa, a Fe<sup>3+</sup>-carbonate of Fe<sub>4</sub>(CO<sub>4</sub>)<sub>3</sub> composition was observed (Boulard et al., 2012). Hence, the siderite melting curve at upper mantle pressures does not involve a phase transition, has a relatively straight positive Clapeyron slope, and a metastable low pressure end (at which *K* may change more strongly with pressure). We have thus adopted a strategy that neglects possible variations in *K'* at low pressures and fixed *K'* for the liquid to the same value as the solid (i.e. 4). Nevertheless, the thermodynamic analysis was also performed with variable *K'*, but has led to results that were similar to those obtained with constant *K'*.

### 6.3. Equations of state

The thermodynamic standard<sup>1</sup> molar properties Gibbs free energy *G<sub>0</sub>* (J/mol), enthalpy *H<sub>0</sub>* (J/mol), entropy *S<sub>0</sub>* (J/K/mol), volume *V<sub>0</sub>* (J/bar/mol), heat capacity *C<sub>p</sub>* (J/K/mol), thermal expansion  $\alpha_0$  (1/K/mol) and bulk modulus *K<sub>0</sub>* (GPa) of FeCO<sub>3</sub>L (Table 2) were fitted on the basis of the constraints described above.

The strategy is to fit the thermodynamic properties *H<sub>0</sub>*, *S<sub>0</sub>*, *V<sub>0</sub>*,  $\alpha_0$ , and *K<sub>0</sub>* of FeCO<sub>3</sub>L at the equilibrium conditions of melting where *G<sub>siderite</sub>* = *G<sub>FeCO3L</sub>*. For crystalline siderite, *H<sub>0</sub>* and *S<sub>0</sub>* were taken directly from Holland and Powell (2011) but their heat capacity function was modified to converge with the Dulong–Petit limit Eq. (10) at high

<sup>1</sup> Standard state refers to 298.15 K and 1 atm.

**Table 2**  
Standard molar thermodynamic properties of siderite and FeCO<sub>3</sub>L at 1 bar & 298.15 K. G<sub>0</sub> Gibbs free energy; H<sub>0</sub> enthalpy; S<sub>0</sub> entropy; V<sub>0</sub> volume; C<sub>p</sub> heat capacity; α<sub>0</sub> thermal expansivity; K<sub>0</sub> bulk modulus; K' pressure derivative of the bulk modulus.

Phase	G <sub>0</sub> (J)	H <sub>0</sub> (J)	S <sub>0</sub> (J/K)	V <sub>0</sub> (J/bar)	C <sub>p</sub> (J/K)	α <sub>0</sub> (1/K)	K <sub>0</sub> (GPa)	K'
Siderite	−790,037	−762,220	93.3	2.94	83.07	6.44E-05	123.0	4
FeCO <sub>3</sub> L	−766,108	−737,666	95.4	3.18	125.4	6.45E-05	80.23	4

Fitted coefficients of C <sub>p</sub> referred to the polynomial Eq. (16), see text.								
	a	b	c	d				
Siderite	178.8	−3.09E-04	625,431	−1773				
FeCO <sub>3</sub> L	128.5	4.54E-03	246,349	−123.7				

temperature (>2000 K). For the thermal expansivity α(T, P<sub>r</sub>) and the bulk modulus K(T, P<sub>r</sub>) we adopt the approximations of [Holland and Powell \(1998\)](#):

$$\alpha(T, P_r) = \alpha_0 * \left(1 - \frac{10}{\sqrt{T}}\right) \quad (11)$$

$$K(T, P_r) = K_0 \left(1 - 1.5 * 10^{-4} (T - 298.15)\right). \quad (12)$$

Volume at reference pressure is

$$V(T, P_r) = V_0 * \left[1 + \int_{T_r}^T \alpha(T, P_r) dT\right]. \quad (13)$$

The Murnaghan equation of state is used to calculate volume at elevated pressure

$$V(T, P) = V(T, P_r) * \left[1 - K' * \frac{P}{\{K' * P + K(T, P_r)\}}\right]^{1/K'} \quad (14)$$

(where K' is the pressure derivative of the bulk modulus).

The volumetric data V<sub>0</sub> = 2.94 J/bar/mol, α<sub>0</sub> = 6.44E-05 1/K/mol, K<sub>0</sub> = 123 GPa and K' = 4 of siderite ([Table 2](#)) are adopted from [Merlini et al. \(submitted for publication\)](#), derived from high temperature and high pressure diamond cell synchrotron X-ray powder diffraction experiments up to 850 °C and 40 GPa. These compressibility data are almost identical to the K<sub>0</sub> = 120(2) GPa and K' = 3.57(9) obtained by [Litasov et al. \(2013\)](#) by synchrotron X-ray diffraction experiments with a multianvil apparatus.

High temperature C<sub>p</sub>-values of siderite (above 2000 K) are calculated using the expanded form of Eq. (10), which becomes (substituting Eq. (11), (12) and (13)):

$$C_p = 3 * R * n + \alpha_0^2 \left(1 - \frac{10}{\sqrt{T}}\right)^2 V_0 \left(1 + 20 * \alpha_0 \sqrt{T_r} - 20 \alpha_0 \sqrt{T} + \alpha_0 T - \alpha_0 T_r\right) * \left(15\right) \\ K_0 (1 - 0.00015 * T + 0.00015 * T_r) * T.$$

Respecting the low temperature C<sub>p</sub> data to 700 K of crystalline siderite ([Holland and Powell, 2011](#)) and the Dulong–Petit convergence criterion at ≥2000 K (Eq. (15)), we fit new coefficients of the isobaric heat capacity C<sub>p</sub> of crystalline siderite ([Table 2](#)) using the polynomial adopted by [Holland and Powell \(2011\)](#)

$$C_p = a + b * T + \frac{c}{T^2} + \frac{d}{\sqrt{T}}. \quad (16)$$

At the P–T conditions of reaction 6 the Gibbs free energy of crystalline siderite (G<sub>FeCO<sub>3</sub></sub>) is calculated from

$$G(P, T) = G(P_r, T_r) - \int_{P_r, T_r}^{P, T} S(P_r, T) dT + \int_{P_r, T}^{P, T} V(P, T) dP.$$

Solving at equilibrium conditions ΔG = 0 = G<sub>FeCO<sub>3</sub>L</sub> − G<sub>siderite</sub> yields the requested standard thermodynamic properties of FeCO<sub>3</sub>L by a non-linear least-square fit to the P–T-polynomial describing the melting curve. The C<sub>p</sub>-values of FeCO<sub>3</sub>L are calculated with Eq. (15) by using the newly fitted volumetric properties V<sub>0</sub>, α<sub>0</sub> and K<sub>0</sub>. The resultant standard thermodynamic molar properties and fitted C<sub>p</sub> coefficients of siderite and FeCO<sub>3</sub>L are summarized in [Table 2](#), plotted C<sub>p</sub> functions for siderite and FeCO<sub>3</sub>L are given in Fig. A1 (Supplementary data).

The calculated melting reaction 6 fits the polynomial Eq. (9) from 5 to 20 GPa within a few degrees, that is largely within error, and is drawn in [Fig. 3](#). Note that the polynomial of Eq. (9) is only valid from 5 to 20 GPa.

## 7. Discussion

### 7.1. Bracketing of the siderite decomposition reaction

The redox dissociation of siderite (reaction 2) has been well studied at pressures to 1 GPa by [French \(1971\)](#) and [Weidner \(1972\)](#) and then by [Tao et al. \(2013\)](#) at 2.5, 4 and 6 GPa ([Fig. 1](#)). Our own experiments (aimed at melting siderite) confirm a decomposition temperature of 1400–1450 °C at 6 GPa. One difficulty in determining both the subsolidus and the melting breakdown reactions of siderite is the incompleteness of reaction in the experiments. For example, [Tao et al.](#) used a natural siderite starting material with ~10% hematite (the latter reacting to ~15% magnetite in the experiments). They established reaction overstepping by the dominant phase abundances, e.g. more than 75 vol.% magnetite would indicate the initiation of decomposition. The small amounts of magnetite present in all experiments of [Tao et al.](#) have been interpreted as a redox product of hematite in the starting material according to reaction 5 whose equilibrium conditions are long overstepped at temperatures of the terminal siderite breakdown (reaction 2). Such equilibrium magnetite is not observed in our experiments. Nevertheless, the melting temperature at 10 GPa and 1550 °C and melt fraction (~25%) determined by [Tao et al. \(2013\)](#) is comparable to our data (at 1600 °C ~70% melt). In their experiments, siderite melts over a temperature interval of ~50 °C, whereas we observe, in particular with increasing pressure, wider melting intervals spanning ~100–150 °C. According to our observations, the melting itself hence involves also equilibria 7 and 8, i.e. the net-melting reaction is (partially) incongruent, resulting in <10% ferric iron components.

Our experiments on siderite at 6 GPa encountered the decomposition reaction 2 at 1450 °C, before the melting temperature was reached, while [Tao et al., 2013](#) observed melting of magnetite + siderite

resulting in a dendritic quench of  $\text{FeCO}_3\text{L}$  at these run conditions. In their experiments, the actual siderite decomposition starts at 1350 °C. This temperature shift of ~100 °C is easily explained by the absence of an internal graphite buffer in Tao et al.'s starting material. The maximum temperature stability of siderite is achieved exactly on the CCO buffer (see below, Fig. 5). A deviation to higher oxygen fugacities (caused by hematite in the Tao et al. starting material) may lead to significantly lower initial breakdown temperatures of siderite although with reaction progress, graphite will be produced and the bulk system will move onto the CCO buffer.

7.2. Calculation of phase relations in Fe–C–O involving siderite

7.2.1. Subsolidus reactions involving siderite breakdown

The experimental results on siderite stability are compared to computed reactions in Fig. 3. For the latter we used *Perple\_X* 6.6.9 (Connolly, 2009) using the siderite volume EoS of Table 2, the calculated melt properties and the fluid equation of state for  $\text{CO}_2$  from Pitzer and Sterner (1994). Changing  $V_0$ ,  $\alpha_0$ , and  $K_0$  of siderite slightly has no significant effect on the internal consistency of the Holland and Powell database. This consistency was established on the basis of experiments

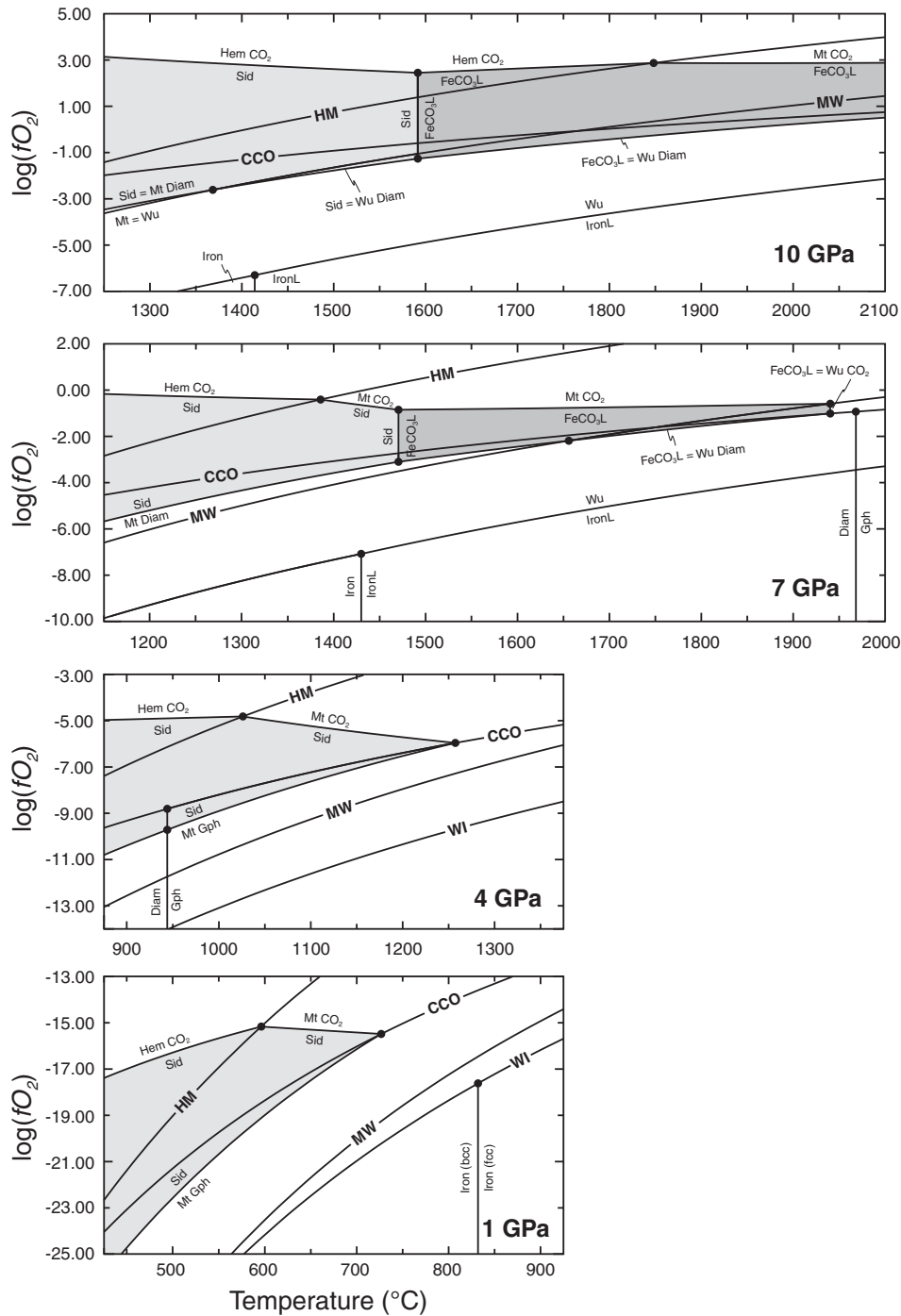


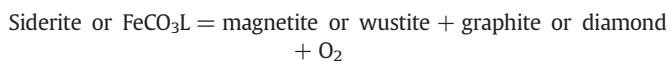
**Fig. 5.** Calculated  $T$ - $f\text{O}_2$  diagrams in the Fe–C–O<sub>2</sub> system in isobaric sections at 1, 4, 7, and 10 GPa, showing siderite (gray) and  $\text{FeCO}_3\text{L}$  (dark gray) stability fields and intersections with the CCO, hematite–magnetite (HM) and magnetite–wüstite (MW) buffers. The maximum stability of siderite or  $\text{FeCO}_3\text{L}$  occurs at the intersection of the siderite/ $\text{FeCO}_3\text{L}$  delimiting reaction with the CCO buffer. Note that in the Fe–C–O<sub>2</sub> system also carbides would occur in the vicinity of the iron–wüstite buffer, these are not included in this calculation. Abbreviations as in Fig. 1.

on siderite at low pressures and temperatures (<750 °C, <1.5 GPa) and our changes introduce a shift in the reaction temperature of <5 °C at these conditions. The experimental brackets, and the calculated terminal siderite stability (reaction 2) are in good agreement with the experiments at low pressures (to 1.5 GPa) but a discrepancy of ~50 to ~100 °C results at 2.5 to 6 GPa. Also the calculated equilibrium (reaction 5), involving siderite + hematite (Fig. 1), coincides within a few degrees with the experimental brackets, confirming that the discrepancy is one of high pressure and temperature. This discrepancy is slightly less (10–20 °C) for the siderite volume properties used by Holland and Powell (2011) than for the data adopted here, but remains a significant problem. One possible explanation stems from the fact that in the calculations, CO<sub>2</sub> has an activity of unity in the fluid, which is probably inadequate with increasing pressures and temperatures as solubilities of Fe in the fluid increase. However, to shift reaction 2 into agreement with the experimental brackets (Fig. 3),  $a_{\text{CO}_2}$  in the fluid would need to be 0.516 when using the fluid EoS of Pitzer and Sterner (1994), which seems unrealistic. Alternatively, other fluid EoS would give results closer in agreement with the experimental brackets, e.g. employing Saxena and Fei (1987) yields a reaction (2) curve now ~25 °C lower than the experimental bracket at 4 GPa (Fig. 3). We conclude that the main uncertainty results from the EoS of CO<sub>2</sub> at >2 GPa, 950 °C and refrain from adopting the caloric thermodynamic properties of siderite.

### 7.2.2. Siderite and FeCO<sub>3</sub>L stability in $P$ - $T$ - $f_{\text{O}_2}$ space

The stability of iron compounds is not only dependent on  $P$ - $T$  conditions, but is also strongly linked to oxygen fugacity ( $f_{\text{O}_2}$ ). We have thus calculated the Fe-C-O<sub>2</sub> phase diagram including siderite, FeCO<sub>3</sub>L, graphite/diamond, a CO<sub>2</sub>-fluid (EoS of Pitzer and Sterner, 1994), the iron oxides (hematite, magnetite, wustite), and iron (fcc, bcc, and melt) in  $T$ - $f_{\text{O}_2}$  sections at 1, 4, 7, and 10 GPa (Fig. 5). The siderite delimiting reactions intersect with the common buffers CCO, wustite-magnetite (MW), and magnetite-hematite (HM) leading at low pressures to a topology similar to that calculated by Yui (1966) and Koziol (2004).

The following topological observations can be made: at any pressure, the siderite or FeCO<sub>3</sub>L stability field has its thermal maximum at the intersection with the CCO buffer. At lower oxygen fugacities, a reaction of the type



limits FeCO<sub>3</sub> stability and is slightly steeper in  $T$ - $f_{\text{O}_2}$  space than the CCO buffer. At oxygen fugacities above the wustite-magnetite and CCO buffers, a reaction of the type



limits FeCO<sub>3</sub> stability and has a subhorizontal slope in  $T$ - $f_{\text{O}_2}$  space. These reactions combined result in a wedge-shaped siderite/FeCO<sub>3</sub>L stability field, tapering off with its maximum temperature on the CCO buffer. This intersection corresponds to the terminal FeCO<sub>3</sub> stability reaction in  $P$ - $T$  space as determined by our graphite saturated experiments. Further complexity in the topology arises when FeCO<sub>3</sub>L is stable to temperatures beyond the crossover of the CCO and magnetite-wustite buffers (~1720 °C at 7 GPa). The FeCO<sub>3</sub>L delimiting reaction then becomes independent of  $f_{\text{O}_2}$  and is



(at 1938 °C, 7 GPa). This latter reaction is calculated to occur at temperatures 450 °C higher than the siderite melting reaction (at 7 GPa), which is limited in significance as the melt in this system would move away from FeCO<sub>3</sub> stoichiometry with increasing temperature.

### 7.2.3. Melting in the Fe-C-O<sub>2</sub> system at low pressures

The thermodynamic data for FeCO<sub>3</sub>L allow calculation of a metastable 1 atm melting temperature of 1012 °C. Nevertheless, at pressures below 6.8 GPa, i.e. the invariant point of Fig. 3, melting occurs through



determined to occur between 1400 and 1450 °C, 6 GPa by Tao et al. (2013). This reaction is the 6 GPa equivalent of the minimum melting reaction in Fe<sub>3</sub>O<sub>4</sub>-C-CO<sub>2</sub> as determined by Weidner (1982) and depicted in Figs. 1 and 3. However, with decreasing pressure, the CO<sub>2</sub> solubility in the melt of reaction 18 and hence the reaction stoichiometry changes, in fact at low pressures this melting reaction involves singularities and is likely to approach an oxide melt at a few kbar (Weidner, 1984).

## 8. Conclusions

In this study we present melting experiments conducted on the siderite system from 6 to 20 GPa and retrieve the thermodynamic properties of FeCO<sub>3</sub>L. The results yield a stable siderite melting curve only from ~6.8 GPa upwards, at temperatures of 1500–1870 °C (at 7–20 GPa). This curve is characterized by a  $P$ - $T$  slope steepening with pressure but without backbend at upper mantle conditions hence the solid remaining denser than the melt.

Siderite melting is not stoichiometric, i.e. leading to a minor ferric oxide melt component and to CO<sub>2</sub> which may or may not dissolve in the melt. The stability of siderite is dependent on  $P$ - $T$ - $f_{\text{O}_2}$  conditions and its thermal maximum terminates at conditions of the CCO buffer. Not unexpectedly, siderite has a lower melting temperature than calcite or magnesite at 7 GPa (Suito et al., 2001; Katsura and Ito, 1990). The siderite melting curve would cross the mantle geotherm at transition zone pressures, where Fe-carbonate melts may infiltrate the deep mantle and would be reduced to immobile diamond as the deep mantle redox state is slightly below the iron-wüstite buffer (Frost and McCammon, 2008; Rohrbach and Schmidt, 2011).

The new standard thermodynamic properties of FeCO<sub>3</sub>L, permit phase equilibrium calculations in the Fe-C-O<sub>2</sub> system, including high pressure melting. Our experimental and thermodynamic data constitute a cornerstone to model carbonate melting in the deep Earth, necessary for understanding the carbon cycle in the mantle.

## Acknowledgments

We thank an anonymous reviewer for the critical comments and suggestions and D. Dingwell for the editorial handling. We also would like to thank C. Liebske for the discussion and technical support in the laboratory. Many thanks to T. Good and B. Zürcher for their mechanical support. This project was funded by the Swiss National Foundation 200020-130100/1 and 200020-140541/1.

## Appendix. Supplementary data

Supplementary data to this article can be found online at <http://dx.doi.org/10.1016/j.chemgeo.2015.02.005>.

## References

- Bale, C., Chartrand, P., Degterov, S.A., Eriksson, G., Hack, K., Ben Mahfoud, R., Melancon, J., Pelton, A.D., Petersen, S., 2002. FactSage thermochemical software and databases. *Calphad* 26, 189–228.
- Berman, R.G., Brown, T.H., 1985. Heat-capacity of minerals in the system Na<sub>2</sub>O-K<sub>2</sub>O-CaO-MgO-FeO-Fe<sub>2</sub>O<sub>3</sub>-Al<sub>2</sub>O<sub>3</sub>-SiO<sub>2</sub>-TiO<sub>2</sub>-H<sub>2</sub>O-CO<sub>2</sub> – representation, estimation, and high-temperature extrapolation. *Contrib. Mineral. Petrol.* 89, 168–183.
- Beukes, N.J., Gutzmer, J., 2008. Origin and paleoenvironmental significance of major iron formations at the Archean-Paleoproterozoic boundary. *Banded Iron Formation-Related High-Grade Iron Ore* 15, pp. 5–47.
- Boulard, E., Menguy, N., Auzende, A.L., Benzerara, K., Bureau, H., Antonangeli, D., Corgne, A., Morard, G., Siebert, J., Perrillat, J.P., Guyot, F., Fiquet, G., 2012. Experimental investigation of the stability of Fe-rich carbonates in the lower mantle. *J. Geophys. Res. Solid Earth* 117.

- Burchard, F., 1924. Bauxite associated with siderite. *Bull. Geol. Soc. Am.* 35, 437–448.
- Burnham, C.W., Davis, N.F., 1974. Role of H<sub>2</sub>O in Silicate Melts. 2. Thermodynamic and phase relations in system NaAlSi<sub>3</sub>O<sub>8</sub>–H<sub>2</sub>O to 10 kilobars, 700 degrees centigrade to 1100 degrees centigrade. *Am. J. Sci.* 274, 902–940.
- Connolly, J.A.D., 2005. Computation of phase equilibria by linear programming: a tool for geodynamic modeling and its application to subduction zone decarbonation. *Earth Planet. Sci. Lett.* 236, 524–541.
- Connolly, J.A.D., 2009. The geodynamic equation of state: what and how. *Geochem. Geophys. Geosyst.* 10.
- Davidson, P.M., Symmes, G.H., Cohen, B.A., Reeder, R.J., Lindsley, D.H., 1993. Synthesis of the new compound CaFe(CO<sub>3</sub>)<sub>2</sub> and experimental constraints on the (Ca, Fe)CO<sub>3</sub> join. *Geochim. Cosmochim. Acta* 57, 5105–5109.
- Franzolin, E., Schmidt, M.W., Poli, S., 2011. Ternary Ca–Fe–Mg carbonates: subsolidus phase relations at 3.5 GPa and a thermodynamic solid solution model including order/disorder. *Contrib. Mineral. Petrol.* 161, 213–227.
- French, B.M., 1970. Stability relations of siderite (FeCO<sub>3</sub>), determined in controlled f<sub>O2</sub> atmospheres. *Goddard Space Flight Center, NASA Doc. X-644-70-102* (61 pp.).
- French, B.M., 1971. Stability relations of siderite (FeCO<sub>3</sub>) in system Fe–C–O. *Am. J. Sci.* 271, 37–78.
- French, B.M., Rosenberg, P.E., 1965. Siderite (FeCO<sub>3</sub>) – thermal decomposition in equilibrium with graphite. *Science* 147, 1283–1284.
- Frost, D.J., McCammon, C.A., 2008. The redox state of Earth's mantle. *Annu. Rev. Earth Planet. Sci.* 36, 389–420.
- Ghiorso, M.S., Sack, R.O., 1995. Chemical mass-transfer in magmatic processes. 4. A revised and internally consistent thermodynamic model for the interpolation and extrapolation of liquid–solid equilibria in magmatic systems at elevated-temperatures and pressures. *Contrib. Mineral. Petrol.* 119, 197–212.
- Goldsmith, J.R., Graf, D.L., Witters, J., Northrop, D.A., 1962. Studies in the system CaCO<sub>3</sub>–MgCO<sub>3</sub>–FeCO<sub>3</sub>. 1. Phase relations. 2. A method for major-element spectrochemical analysis. 3. Compositions of some Ferroan dolomites. *J. Geol.* 70, 659–688.
- Griggs, D.T., Kennedy, G.C., 1956. A simple apparatus for high pressures and temperatures. *Am. J. Sci.* 254, 722–735.
- Gualda, G.A.R., Ghiorso, M.S., Lemons, R.V., Carley, T.L., 2012. Rhyolite–MELTS: a modified calibration of MELTS optimized for silica-rich, fluid-bearing magmatic systems. *J. Petrol.* 53, 875–890.
- Harker, R.L., Tuttle, O.F., 1955. Studies in the system CaO–MgO–CO<sub>2</sub>. 1. The thermal dissociation of calcite, dolomite and magnesite. *Am. J. Sci.* 253, 209–224.
- Holland, H.D., 1965. Some applications of thermochemical data to problems of ore deposits. II. Mineral assemblages and the composition of ore-forming fluids. *Econ. Geol.* 60, 1101–1166.
- Holland, T.J.B., Powell, R., 1998. An internally consistent thermodynamic data set for phases of petrological interest. *J. Metamorph. Geol.* 16, 309–343.
- Holland, T.J.B., Powell, R., 2001. Calculation of phase relations involving haplogranitic melts using an internally consistent thermodynamic dataset. *J. Petrol.* 42, 673–683.
- Holland, T.J.B., Powell, R., 2011. An improved and extended internally consistent thermodynamic dataset for phases of petrological interest, involving a new equation of state for solids. *J. Metamorph. Geol.* 29, 333–383.
- Irving, A.J., Wyllie, P.J., 1975. Subsidiolus and melting relationships for calcite, magnesite and join CaCO<sub>3</sub>–MgCO<sub>3</sub> to 36 Kb. *Geochim. Cosmochim. Acta* 39, 35–53.
- Katsura, T., Ito, E., 1990. Melting and subsolidus phase-relations in the MgSiO<sub>3</sub>–MgCO<sub>3</sub> system at high-pressures – implications to evolution of the earth's atmosphere. *Earth Planet. Sci. Lett.* 99, 110–117.
- Klement, W., Cohen, L.H., 1975. Solid–solid and solid–liquid transitions in K<sub>2</sub>CO<sub>3</sub>, Na<sub>2</sub>CO<sub>3</sub> and Li<sub>2</sub>CO<sub>3</sub> – investigations to greater than – 5 kbar by differential thermal-analysis – thermodynamics and structural correlations. *Ber. Bunsenges. Phys. Chem.* 79, 327–334.
- Klemm, D.D., 2000. The formation of Palaeoproterozoic banded iron formations and their associated Fe and Mn deposits, with reference to the Griqualand West deposits, South Africa. *J. Afr. Earth Sci.* 30, 1–24.
- Kozioł, A.M., 2004. Experimental determination of siderite stability and application to Martian meteorite ALH84001. *Am. Mineral.* 89, 294–300.
- Kusky, T.M., Li, J.H., Tucker, R.D., 2001. The Archean Dongwanzi ophiolite complex, North China craton: 2.505-billion-year-old oceanic crust and mantle. *Science* 292, 1142–1145.
- Litasov, K.D., Shatskiy, A., Gavryushkin, P.N., Sharygin, I.S., Dorogokupets, P.I., Dymshits, A.M., Ohtani, E., Higo, Y., Funakoshi, K., 2013. P–V–T equation of state of siderite to 33 GPa and 1673 K. *Phys. Earth Planet. Inter.* 224, 83–87.
- Liu, Q., Tenner, T.J., Lange, R.A., 2007. Do carbonate liquids become denser than silicate liquids at pressure? Constraints from the fusion curve of K<sub>2</sub>CO<sub>3</sub> to 3.2 GPa. *Contrib. Mineral. Petrol.* 153, 55–66.
- Marcus, Y., 2009. Heat capacities of molten salts with polyatomic anions. *Thermochim. Acta* 495, 81–84.
- Marcus, Y., 2013. The compressibility of molten salts. *J. Chem. Thermodyn.* 61, 7–10.
- Medard, E., Grove, T.L., 2008. The effect of H<sub>2</sub>O on the olivine liquids of basaltic melts: experiments and thermodynamic models. *Contrib. Mineral. Petrol.* 155, 417–432.
- Merlini, M., Tumati, S., Lotti, P., Sapelli, F., Fumagalli, P., Gatta, D., Abdellatif, M., Plaisier, J., Lausi, A., Hanfland, M., Crichton, W., Chantel, J., Guignard, J., Pavese, A., Poli, S., 2015. High temperature and high pressure behavior of carbonates in the ternary diagram CaCO<sub>3</sub>–MgCO<sub>3</sub>–FeCO<sub>3</sub>. *Am. Mineral.* (submitted for publication).
- Morishima, H., Kato, T., Suto, M., Ohtani, E., Urakawa, S., Utsumi, W., Shimomura, O., Kikegawa, T., 1994. The phase-boundary between alpha-Mg<sub>2</sub>SiO<sub>4</sub> and beta-Mg<sub>2</sub>SiO<sub>4</sub> determined by in-situ X-ray-observation. *Science* 265, 1202–1203.
- O'Leary, M.C., Lang, R.A., Ai, Y., 2009. The compressibility of K<sub>2</sub>CO<sub>3</sub>–Na<sub>2</sub>CO<sub>3</sub>–Li<sub>2</sub>CO<sub>3</sub>–CaCO<sub>3</sub> liquids derived from sound speed measurements: implications for the fusion curve of CaCO<sub>3</sub>. *American Geophysical Union, Fall Meeting 2009, abstract #V11D-1990*.
- Pal'yanov, Y.N., Sokol, A.G., Borzdov, Y.M., Khokhryakov, A.F., Shatsky, A.F., Sobolev, N.V., 1999. The diamond growth from Li<sub>2</sub>CO<sub>3</sub>, Na<sub>2</sub>CO<sub>3</sub>, K<sub>2</sub>CO<sub>3</sub> and Cs<sub>2</sub>CO<sub>3</sub> solvent-catalysts at P = 7 GPa and T = 1700–1750 degrees C. *Diam. Relat. Mater.* 8, 1118–1124.
- Phillips, B., Muan, A., 1959. Phase equilibria in the system CaO–iron oxide–SiO<sub>2</sub> in air. *J. Am. Ceram. Soc.* 42, 413–423.
- Pitzer, K.S., Sterner, S.M., 1994. Equations of state valid continuously from zero to extreme pressures for H<sub>2</sub>O and CO<sub>2</sub>. *J. Chem. Phys.* 101, 3111–3116.
- Polat, A., Hofmann, A.W., Rosing, M.T., 2002. Boninite-like volcanic rocks in the 3.7–3.8 Ga Isua greenstone belt, West Greenland: geochemical evidence for intra-oceanic subduction zone processes in the early Earth. *Chem. Geol.* 184, 231–254.
- Poli, S., Franzolin, E., Fumagalli, P., Crottini, A., 2009. The transport of carbon and hydrogen in subducted oceanic crust: an experimental study to 5 GPa. *Earth Planet. Sci. Lett.* 278, 350–360.
- Richet, P., Bottinga, Y., 1980. Heat-capacity of liquid silicates – new measurements on NaAlSi<sub>3</sub>O<sub>8</sub> and K<sub>2</sub>Si<sub>4</sub>O<sub>9</sub>. *Geochim. Cosmochim. Acta* 44, 1535–1541.
- Rohrbach, A., Schmidt, M.W., 2011. Redox freezing and melting in the Earth's deep mantle resulting from carbon–iron redox coupling. *Nature* 472, 209–212.
- Rosenberg, P.E., 1963. Subsidiolus relations in system CaCO<sub>3</sub>–FeCO<sub>3</sub>. *Am. J. Sci.* 261, 683–690.
- Rosenberg, P.E., 1967. Subsidiolus relations in system CaCO<sub>3</sub>–MgCO<sub>3</sub>–FeCO<sub>3</sub> between 350 degrees and 550 degrees C. *Am. Mineral.* 52, 787–796.
- Santillan, J., Williams, Q., 2004. A high-pressure infrared and X-ray study of FeCO<sub>3</sub> and MnCO<sub>3</sub>: comparison with CaMg(CO<sub>3</sub>)<sub>2</sub>-dolomite. *Phys. Earth Planet. Inter.* 143, 291–304.
- Saxena, S.K., Fei, Y., 1987. High-pressure and high-temperature fluid fugacities. *Geochim. Cosmochim. Acta* 51, 783–791.
- Schneider, C.A., Rasband, W.S., Eliceiri, K.W., 2012. NIH Image to ImageJ: 25 years of image analysis. *Nat. Methods* 9, 671–675.
- Seguin, M., 1966. Instability of FeCO<sub>3</sub> in air. *Am. J. Sci.* 264, 562–568.
- Shatskiy, A., Sharygin, I.S., Gavryushkin, P.N., Litasov, K.D., Borzdov, Y.M., Shcherbakova, A.V., Higo, Y., Funakoshi, K., Pal'yanov, Y.N., Ohtani, E., 2013. The system K<sub>2</sub>CO<sub>3</sub>–MgCO<sub>3</sub> at 6 GPa and 900–1450 degrees C. *Am. Mineral.* 98, 1593–1603.
- Silliman, B., 1820. Sketches of a tour in the counties of New Haven and Litchfield. *Am. J. Sci.* 2, 201–235.
- Sleep, N.H., Zahnle, K., 2001. Carbon dioxide cycling and implications for climate on ancient Earth. *J. Geophys. Res. Planets* 106, 1373–1399.
- Smythe, J.A., Dunham, K.C., 1947. Ankerites and chalybites from the northern Pennine ore-field and the north-east coalfield. *Mineral. Mag.* 28, 53–74.
- Staudigel, H., 2003. 3.15 – Hydrothermal Alteration Processes in the Oceanic Crust. In *Treatise on Geochemistry*, eds. D. H. Editors-in-Chief: Heinrich & K. T. Karl, 511–535. Oxford: Pergamon.
- Stewart, A.J., van Westrenen, W., Schmidt, M.W., Melekhova, E., 2006. Effect of gasketing and assembly design: a novel 10/3.5 mm multi-anvil assembly reaching perovskite pressures. *High Pressure Res.* 26, 293–299.
- Suito, K., Namba, J., Horikawa, T., Taniguchi, Y., Sakurai, N., Kobayashi, M., Onodera, A., Shimomura, O., Kikegawa, T., 2001. Phase relations of CaCO<sub>3</sub> at high pressure and high temperature. *Am. Mineral.* 86, 997–1002.
- Susaki, J., Akaogi, M., Akimoto, S., Shimomura, O., 1985. Garnet–perovskite transformation in Cageo3 – Insitu X-ray measurements using synchrotron radiation. *Geophys. Res. Lett.* 12, 729–732.
- Tao, R.B., Fei, Y.W., Zhang, L.F., 2013. Experimental determination of siderite stability at high pressure. *Am. Mineral.* 98, 1565–1572.
- Weidner, J.R., 1972. Equilibria in system Fe–C–O. 1. Siderite–magnetite–carbon–vapor equilibrium from 500 to 10,000 bars. *Am. J. Sci.* 272, 735–751.
- Weidner, J.R., 1982. Iron-oxide magmas in the system Fe–C–O. *Can. Mineral.* 20, 555–566.
- Weidner, J.R., 1984. Equilibria in the system Fe–C–O and the origin of native iron. *Can. Mineral.* 22, 347–356.
- Wyllie, P.J., 1979. Magmas and volatile components. *Am. Mineral.* 64, 469–500.
- Wyllie, P.J., Tuttle, O.F., 1960. The system CaO–CO<sub>2</sub>–H<sub>2</sub>O and the origin of carbonatites. *J. Petrol.* 1, 1–46.
- Yagi, T., Akimoto, S.I., 1976. Direct determination of coesite–stishovite transition by in situ X-ray measurements. *Tectonophysics* 35, 259–270.
- Yui, S., 1966. Decomposition of siderite to magnetite at lower oxygen fugacities – a thermochemical interpretation and geological implications. *Econ. Geol.* 61, 768–776.
- Zhang, J., Li, B., Utsumi, W., Liebermann, R.C., 1996. In situ X-ray observations of the coesite stishovite transition: reversed phase boundary and kinetics. *Phys. Chem. Miner.* 23, 1–10.
- Zhu, H.-M., Saito, T., Sato, Y., Yamamura, T., Shimakage, K., Ejima, T., 1991. Ultrasonic velocity and absorption coefficient in molten alkali metal nitrates and carbonates. *J. Jpn. Inst. Metals* 55, 937–944.